CHEMISTRY OF MATERIALS
Cite This: Chem. Mater. 2019, 31, 8000−8011
Article
pubs.acs.org/cm

Light-Driven, Facet-Selective Transformation of Cuprous Oxide Microcrystals to Hollow Copper Nanoshells

Chu Qin,[†] Brandon M. Campbell,[†] Meikun Shen,[†] Tong Zhao,[†] and Bryce Sadtler*[,†,‡]

[†]Department of Chemistry and [‡]Institute of Materials Science & Engineering, Washington University, St. Louis, Missouri 63130, United States

Supporting Information

ABSTRACT: Photoexcitation can be used to control the composition and nanoscale morphology of inorganic materials. Here we report the photoinduced transformation of faceted cuprous oxide (Cu_2O) microcrystals to hollow particles consisting of an inner region of cuprous oxide and an outer shell of copper metal. When cuprous oxide microcrystals with mixed {100} and {111} facets are held at a negative bias (−1.0 V vs Ag/AgCl) in a solution of sodium hydroxide (NaOH), light mediates the growth of copper metal selectively on the {100} facets while the crystal interior is etched at {111} facets. Conformal Cu layers grow to connect at vertices of the cuboctahedral microcrystals and form a hollow shell. This process is only observed in the presence of illumination. Without an applied bias the {100} facets are preferentially etched under illumination in the same NaOH solution. We propose this light-driven, facet-selective transformation arises from the potential-dependent structure and energetics of the semiconductor/electrolyte interface, which lead to facet-selective extraction of photogenerated electrons from the {100} facets when the applied bias is more negative than the flat-band potential of the Cu_2O microcrystals. Growth of the Cu shell protects the {100} facets while the {111} facets are chemically etched in the presence of oxygen and hydroxide.

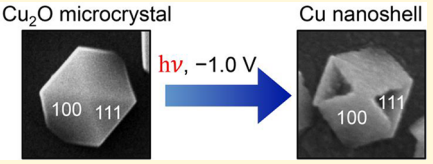

INTRODUCTION

Photochemical and photoelectrochemical reactions use light to drive the formation of chemical products.[1−3] In semiconductors and plasmonic metals, photon-to-chemical conversion is mediated by the generation of mobile charge carriers that can be extracted from the material to oxidize or reduce surface-adsorbed species. The extraction of photoexcited charges can also be used to grow or transform the material itself. Illumination during growth has produced complex nanoscale morphologies in both semiconductors and metals that are difficult to achieve by other synthetic routes.[4,5] A prominent example of light-directed growth is the photoinduced conversion of spherical silver nanoparticles to nanorods and nanoprisms.[5−9] This transformation is initiated by plasmon excitations that decay to generate hot charge carriers.[10−12] Early reports hypothesized the prism and rod shapes resulted from anisotropic electromagnetic fields produced by plasmon excitation that create preferential regions for growth on the initially spherical Ag seed particles.[6,13,14] However, it now appears that the final shape of the Ag nanoparticle is dictated by the specific facets and planar defects (e.g., twin boundaries or stacking faults) present during the early stages of growth.[5−9]

More recently, illumination has been used to drive the formation of complex, nanoscale patterns during the electrochemical growth of chalcogenide glasses.[4,15−20] Light−matter interactions (e.g., absorption and scattering) near the surface of the growing film lead to periodic variations in the concentration of photoexcited charge carriers. Because of the low mobility of charge carriers in chalcogenide glasses,[4,21−23] only photoexcited electrons near the surface of the films can be used to add material via reduction of ions in solution. In this way, the growth of the film mimics the light-intensity pattern and can be controlled by the wavelength, polarization, and angle of the incident illumination.[15−18]

In plasmon-mediated growth of Ag nanoparticles, the structure of the Ag seed particles is believed to be dynamic under illumination, making it difficult to correlate the initial structure with the final particle shape.[8,24] In the photoelectrochemical growth of nanopatterned chalcogenide films, the electrodeposited material is poorly crystalline consisting of nanoscale grains mixed with amorphous material.[15] Thus, the role of surface structure in the resulting morphology during light-directed growth remains underexplored. To expand the range of materials and morphologies that can be grown by using light, we decided to study how illumination affects the electrochemical growth of a material system that exhibits highly facet-dependent chemical and physical properties. Cu_2O microcrystals serve as a model system for this work as they exhibit facet-dependent growth,[25−31] catalytic activity,[29−36] stability,[37−40] and surface reactivity.[41−46] In these previous reports, facet effects have been attributed to the relative surface energies of different facets, the passivation of specific facets through selective binding agents, the facet-selective extraction of mobile charge carriers, and the facet-selective adsorption of reactive chemical species.

Received: June 7, 2019
Revised: September 6, 2019
Published: September 9, 2019

Downloaded via WASHINGTON UNIV on October 20, 2019 at 19:54:34 (UTC).
See https://pubs.acs.org/sharingguidelines for options on how to legitimately share published articles.

© 2019 American Chemical Society

DOI: 10.1021/acs.chemmater.9b02240
Chem. Mater. 2019, 31, 8000−8011

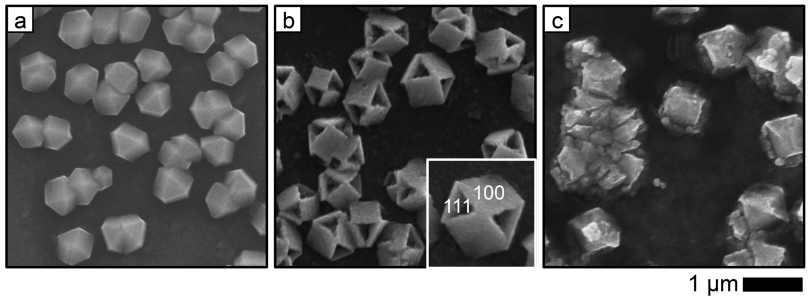

Figure 1. Electrochemical transformation of Cu_2O microcrystals under illumination and in the dark. (a) SEM image of the initial Cu_2O microcrystals electrodeposited on a Au substrate. (b) Cu_2O microcrystals after 5 min of illumination with an ELH lamp while the electrode was held at a constant potential of $E = -1.0$ V vs Ag/AgCl in 5 M NaOH. The inset shows a magnified image of a single hollow nanoshell with the {100} and etched {111} facets labeled. (c) Cu_2O microcrystals after 5 min of being held at the same potential in 5 M NaOH in the dark.

Previous work has shown that illumination catalyzes the growth of Cu nanowires on Cu_2O microcrystals[47] and can be used to prepare n-type Cu_2O films that are doped with Cu^0.[48,49] However, neither of these prior examples studied the facet dependence of these photochemical reactions. In this report, we examined both the oxidative etching of Cu_2O and the reductive deposition of Cu on Cu_2O microcrystals that possess a mixture of {100} and {111} facets. Using a combination of illumination and an applied bias, both of these reactions occur selectively on {100} facets but at different potential windows. We develop a physical mechanism to explain these light-driven transformations, which relies on facet-selective ion adsorption and extraction of photogenerated charge carriers. By controlling these processes, we synthesized a novel nanoscale morphology consisting of a shell of Cu metal deposited selectively on the {100} facets of the initial Cu_2O microcrystals. The interior either is hollow or contains Cu_2O depending on the growth time.

RESULTS

Arrays of Cu_2O microcrystals on conductive substrates were prepared by electrodeposition under controlled current conditions following modifications to previously reported procedures.[26,27] Both the waveform of the deposition current vs time and the addition of facet-selective binding agents (sodium dodecyl sulfate and chloride ions) were used to tune the ratio of {100} to {111} facets. The conditions used to grow Cu_2O microcrystals of different morphologies are provided in detail in the Experimental Section. A scanning electron microscopy (SEM) image of cuboctahedral microcrystals with mixed {100} and {111} facets is shown in Figure 1a. The facets can be distinguished by their symmetry as {111} facets with 3-fold rotational symmetry appear as triangles or as triangles with truncated corners. The {100} facets with 4-fold rotational symmetry appear as squares or squares with truncated corners. An X-ray diffraction (XRD) pattern of the initial Cu_2O microcrystals electrodeposited on a Au substrate is shown in Figure 2 (blue trace). The strongest reflection at 38° in 2θ belongs to the Au substrate as the deposited microcrystals are relatively sparse on the substrate. However, the peaks at 29° and 36° in 2θ match the {110} and {111} reflections for the cubic phase of Cu_2O (see Figure S9 in the Supporting Information for a XRD pattern of the Cu_2O microcrystals over a wider 2θ range). The {200} reflection for Cu_2O at 42° is likely absent due to the preferential alignment of {111} planes parallel to the substrate. SEM images of Cu_2O microcrystals with predominantly {100} facets and predominantly {111} facets are shown in Figures 5a and 5c, respectively. Cyclic voltammetry (CV) of the microcrystals shows a cathodic peak at −0.41 vs silver/silver chloride (Ag/AgCl) corresponding to the reduction of Cu_2O to Cu metal (Figures S2 and S3).[50] The reduction of adsorbed oxygen also occurs on the exposed regions of the Au substrate (Figure S1).

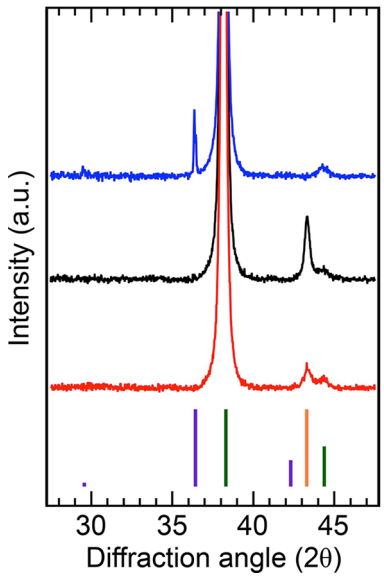

Figure 2. X-ray diffraction patterns of the initial Cu_2O microcrystals electrodeposited on a Au substrate (blue trace, top), Cu_2O microcrystals after 5 min while the electrode was held at a constant potential of $E = -1.0$ V vs Ag/AgCl in 5 M NaOH in the dark (black trace, middle), and Cu_2O microcrystals after 5 min of illumination with an ELH lamp while the electrode was held at the same potential in 5 M NaOH (red trace, bottom). The lines at the bottom are the reflections for standard XRD powder patterns of Cu_2O (purple lines, PDF file #04-007-9767), Cu (orange line, PDF file #00-004-0836), and Au (green lines, PDF file #00-004-0784).

Previous reports have shown that changes in the local pH and potential can induce either oxidation or reduction of Cu_2O.[26,27,39,51−53] We found that these chemical transformations are significantly altered in the presence of illumination. Figure 1 shows SEM images of the Cu_2O microcrystals grown on Au after the substrates were held at a potential of $E = -1.0$ V vs Ag/AgCl in a solution of 5 M NaOH both under illumination (Figure 1b) and in the dark (Figure 1c). An ELH-style halogen lamp was used as the light source, and the typical irradiance at the electrode was between 300 and 655 mW/cm^2. Under illumination, hollow structures

DOI: 10.1021/acs.chemmater.9b02240
Chem. Mater. 2019, 31, 8000−8011

are formed in which a shell has grown selectively on the {100} facets while the interiors of the microcrystals have been etched at {111} facets. As shown in Figure 1c, the hollow nanoshells are not formed in the dark. Illuminating the electrode increases the current when it is held at −1.0 V vs Ag/AgCl (Figure S4). However, simply increasing the current density in the dark (either through applying a more negative potential or under constant current conditions) did not lead to the nanoshell formation (Figure S5). The threshold irradiance to observe the formation of the hollow nanoshells was 50 mW/cm^2 with an ELH lamp (Figure S7). At lower light intensities, etching of the microcrystals in the NaOH solution outcompetes growth of the shells, resulting in broken particles (Figure S7). While a broadband ELH lamp was used for most experiments, we also used narrow-band (full width at half-maximum of ∼30 nm) light-emitting diodes (LEDs) with wavelengths of 455 and 625 nm. Based on its band gap energy of 2.1 eV, Cu_2O strongly absorbs blue light (see Figure S6 for an absorption spectrum of the Cu_2O microcrystals). Correspondingly, illumination with the 455 nm LED produced the same hollow nanoshells as when the ELH lamp was used (Figure S8a). However, as Cu_2O does not significantly absorb red light, the 625 nm LED produced structures similar to those formed in the dark (Figure S8b).

The combination of an applied potential and exposure to the NaOH solution led to compositional changes in the Cu_2O microcrystals both under illumination and in the dark. We monitored these changes using XRD and X-ray photoelectron spectroscopy (XPS). XRD showed that after applying a bias of −1.0 V vs Ag/AgCl for 5 min while the microcrystals were immersed in 5 M NaOH (both in the dark and under illumination), a reflection at 43° in 2θ corresponding to Cu metal appeared in the diffraction patterns while the peaks at 29° and 36° belonging to Cu_2O disappeared (Figure 2). Figure S9 provides XRD patterns over a wider 2θ range. The presence of Cu metal on the surface of the microcrystals was also verified by X-ray photoelectron spectroscopy in the Auger region for Cu LMM electrons (Figure 3b and Figure S11). Before and after the transformation, the samples possessed a peak with a kinetic energy of 916.8 eV indicative of Cu^+. After the transformation in both the light and dark, a new peak appeared at 918.5 eV corresponding to metallic Cu^0.[54,55]

Based on SEM images, etching still occurs even when the microcrystals are held at a negative bias. As described further below, the combination of OH^- ions and dissolved O_2 in the electrolyte solution leads to oxidation of Cu_2O microcrystals similar to previous reports.[39] The presence of Cu^{2+} cannot be easily identified in the Auger region as it appears at 917.8 eV in between the Cu^+ and Cu^0 peaks. On the other hand, photoelectron spectra in the binding energy region for Cu $2p_{3/2}$ electrons can identify the presence of Cu^{2+} but cannot distinguish between Cu^+ and Cu^0.[54,55] A broad peak with a binding energy of ∼933.4 eV in the Cu $2p_{3/2}$ photoelectron spectra corresponding to Cu^{2+} was observed for all three samples. This peak was the strongest after transformation of the microcrystals in the dark (Figure 3a). The contribution from Cu^{2+} also increased when the microcrystals were immersed in 5 M NaOH in the dark without an applied bias (Figure S10). XPS in the binding energy region for O 1s electrons shows contributions from both oxygen in the Cu_2O microcrystals and surface-adsorbed oxygen species both before and after the applied bias (Figure S12).

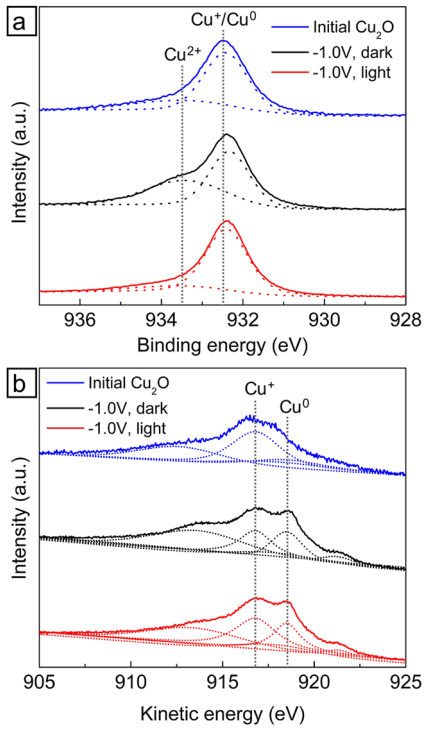

Figure 3. (a) XPS showing the binding energy region for Cu $2p_{3/2}$ electrons. (b) Auger spectra in the region for Cu LMM electrons. In both panels, the blue trace (top) shows the initial Cu_2O microcrystals electrodeposited on a Au substrate, the black trace (middle) shows the Cu_2O microcrystals after 5 min while the electrode was held at a constant potential of E = −1.0 V vs Ag/AgCl in 5 M NaOH in the dark, and the red trace (bottom) shows Cu_2O microcrystals after 5 min of illumination with an ELH lamp while the electrode was held at the same potential in 5 M NaOH. Dashed lines show deconvolution of the peaks as described in the text. The vertical lines indicate the expected energies for Cu in the 0, +1, and +2 oxidation states based on previous assignments.[54,55] Peaks at 913 and 921 eV in the Auger spectra have been observed previously for Cu_2O but have not been assigned to a particular oxidation state.[54]

Figure 4 shows the evolution of the microcrystals under illumination as a function of time while the substrate was held at E = −1.0 V vs Ag/AgCl in 5 M NaOH. In the first minute of the reaction Cu nanoparticles grow on the {100} facets of the Cu_2O microcrystals (Figure 4a). At longer deposition times the Cu nanoparticles grow and merge into polycrystalline layers covering the {100} facets. The Cu layers formed on different {100} facets connect at the vertices of each cuboctahedral microcrystal (Figure 4b). After 2.5 min the Cu_2O surfaces exposed at {111} facets have begun to etch in the NaOH solution (Figure 4c). The Cu shell is resistant to etching while the interiors of the Cu_2O microcrystals are hollowed out through further etching at the {111} facets (Figure 4d).

The Cu_2O microcrystals are oxidatively etched by the combination of OH^- ions and O_2 in the electrolyte solution. CV scans of the used NaOH solution showed the presence of Cu^{2+} in solution after the transformation as a result of this etching (Figure S13). However, adding $Cu(NO_3)_2$ intentionally to the deposition solution did not alter the formation of the Cu nanoshells (Figure S14). When the NaOH concentration was lowered to either 2.5 or 1 M, etching of the {111} facets was slower, leading to thicker Cu shells and Cu_2O remaining in the interior of the particles for longer times

DOI: 10.1021/acs.chemmater.9b02240
Chem. Mater. 2019, 31, 8000−8011

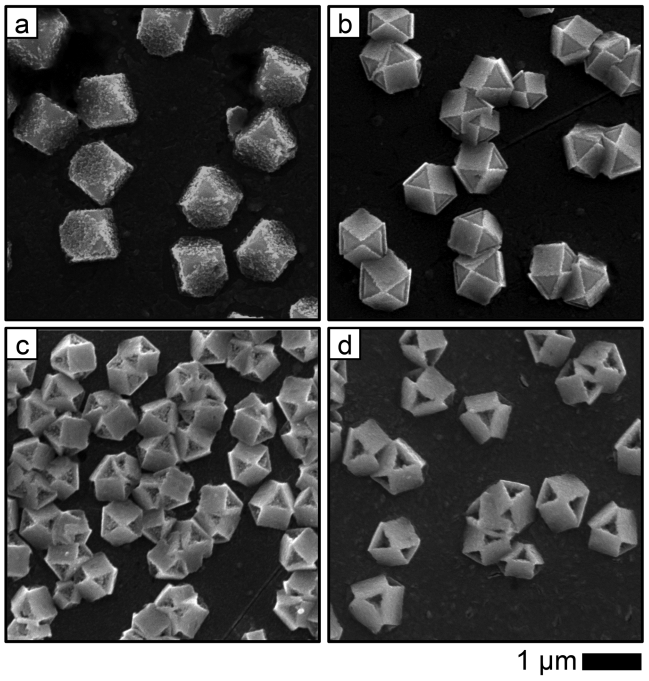

Figure 4. SEM images of Cu_2O microcrystals on Au substrates after (a) 1, (b) 2, (c) 2.5, and (d) 5 min of illumination with an ELH lamp while the electrode was held at a potential of $E = -1.0$ V vs Ag/AgCl in 5 M NaOH.

(Figures S15 and S16). The preparation of the NaOH solution and the transformation of the microcrystals were both typically performed in air. Some hollow nanoshells were still observed under illumination at −1.0 V vs Ag/AgCl when the NaOH solution was purged with argon (Figure S17). However, both the nanoshell formation and etching of the {111} facets were less uniform, indicating that dissolved O_2 is involved in the transformation.

Selective deposition of Cu on {100} facets and etching of the {111} facets occur even when the ratio of these two surfaces is changed. Figure 5 shows SEM images of truncated cubic Cu_2O microcrystals with predominantly {100} facets (Figure 5a), cuboctahedral microcrystals with mixed {100} and {111} facets (Figure 5b), and octahedral microcrystals with predominantly {111} facets (Figure 5c). After the cubic microcrystals were held at −1.0 V vs Ag/AgCl for 5 min under illumination, Cu shells have covered the majority of the surface of the microcrystals. However, the truncated corners corresponding to {111} facets have been etched. Under the same conditions, octahedral microcrystals are converted into hollow frames where Cu has grown on the edges and corners of the original microcrystals.

The hollow nanoshell morphology for particles shown in Figures 1, 4, and 5 is only formed when the applied potential is sufficiently negative. In the absence of an applied potential and at more positive potentials, the {100} facets are selectively etched under illumination. Figure S20 shows selective etching of {100} facets for both electrodeposited and colloidally synthesized Cu_2O microcrystals when illuminated in 5 M NaOH in the absence of an applied bias for 3 and 10 min, respectively. Without either light or an applied bias (i.e., just immersing the microcrystals in 5 M NaOH), etching of the {100} facets was still observed at longer times (20 min), although the etching was not as uniform (Figure S19). Figure 6 shows SEM images of Cu_2O microcrystals after being held for 5 min at a series of different potentials under illumination with an ELH lamp in a solution of 5 M NaOH. At a potential of $E = -0.4$ V vs Ag/AgCl, the {100} facets were selectively etched while no obvious deposition of Cu was observed (Figure 6a). At an applied potential of $E = -0.5$ V vs Ag/AgCl, the {100} facets were still etched, and large Cu particles were deposited nonselectively on the microcrystals (Figure 6b). Figure 6c shows that as the applied potential was made more negative ($E = -0.8$ V vs Ag/AgCl), a Cu shell formed selectively on the {100} facets of the microcrystals. However, the Cu coating

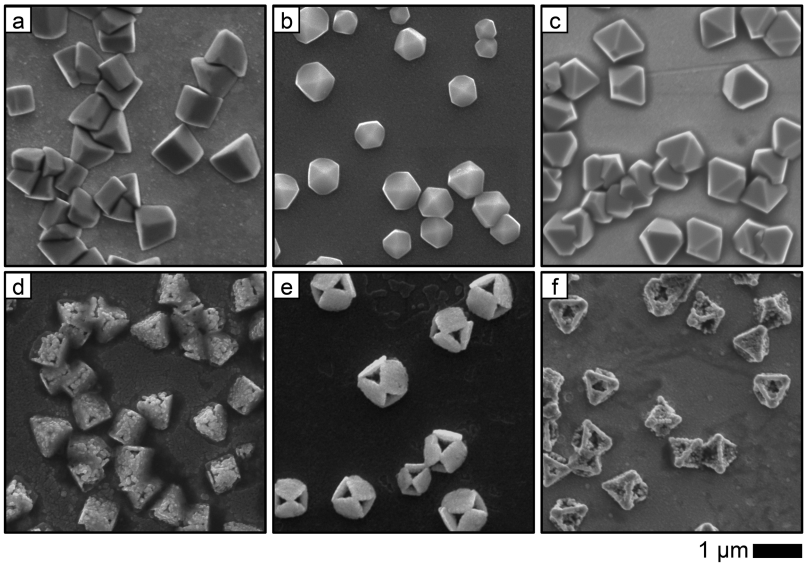

Figure 5. Facet dependence of the photoinduced transformation of Cu_2O microcrystals. (a–c) SEM images of the initial Cu_2O microcrystals with (a) truncated cubic, (b) cuboctahedral, and (c) octahedral morphologies. (d–f) Hollow Cu nanoshells grown from Cu_2O microcrystals with (d) truncated cubic, (e) cuboctahedral, and (f) octahedral morphologies after 5 min of illumination with an ELH lamp while the electrode was held at a constant potential of $E = -1.0$ V vs Ag/AgCl in 5 M NaOH.

DOI: 10.1021/acs.chemmater.9b02240
Chem. Mater. 2019, 31, 8000–8011

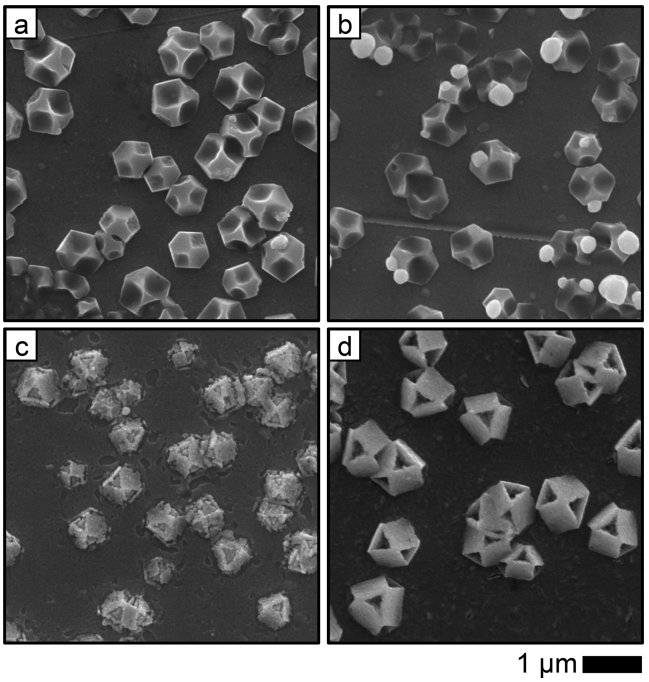

Figure 6. SEM images of Cu_2O microcrystals after being held for 5 min under illumination with an ELH lamp in a solution of 5 M NaOH at potentials of (a) −0.4 V, (b) −0.5 V, (c) −0.8 V, and (d) −1.0 V vs Ag/AgCl.

formed at −0.8 V was not as uniform as when a potential of E = −1.0 V vs Ag/AgCl was used (Figure 6d).

The currents both in the dark and under illumination are shown at different applied potentials in Figure 7. Spikes in the current were observed when the illumination was turned on and off, which have been previously observed for Cu_2O microcrystal photoelectrodes[51] as well as for TiO_2-based, dye-sensitized photoelectrochemical cells.[56−58] Mallouk and co-workers attributed the current spikes to the redistribution of charge carriers among trap states with different energies, while the slower change in current was assigned to surface processes.[58] As we are primarily interested in surface processes (i.e., surface reduction of copper ions and oxidation of Cu_2O), we focus on the changes in current following the initial spikes. Furthermore, regions of the Au electrode are still exposed after growth of the Cu_2O microcrystals, and the reduction of O_2 on the Au substrate leads to a small cathodic background current (see Figure S1). However, as this background current does not change under illumination, we ascribe the changes in current when the electrode is illuminated to result from photo-excitation of the Cu_2O semiconductor microcrystals.

The open-circuit potential for the initial Cu_2O microcrystals in 5 M NaOH is −0.37 V vs Ag/AgCl. At potentials more positive than open circuit (e.g., E = −0.3 V vs Ag/AgCl), the current is anodic (oxidative) in the dark, and the steady-state anodic current (i.e., following the initial spike) is enhanced under illumination (Figure 7a). At potentials more negative than the open-circuit potential, the dark current is negative due to reduction of Cu_2O to Cu (Figure S2). Just as Figure 6b shows photoetching of {100} facets along with nonselective deposition of Cu at E = −0.5 V vs Ag/AgCl, the current trace at this potential (Figure 7b) shows a slightly cathodic (reductive) current in the dark that becomes anodic under illumination. Similar changes in the current were observed at E = −0.4 V vs Ag/AgCl. Choi and co-workers also reported similar changes in current for electrodeposited Cu_2O microcrystals where the current was cathodic in the dark and became anodic under illumination over this potential range.[51] At more negative potentials of E = −0.8 and −1.0 V vs Ag/AgCl, the current is cathodic in the dark, and the steady-state current becomes more negative under illumination (Figure 7c,d). Figure S21 provides the changes in current under illumination at applied potentials of −0.55, −0.60, −0.65, and −0.70 V vs Ag/AgCl. The crossover between when illumination makes the current more positive and when illumination makes the current more negative occurs between −0.60 and −0.65 V vs Ag/AgCl.

DISCUSSION

Compositional Changes in Cu_2O Microcrystals. The following half-reactions control the oxidation and reduction of Cu_2O:

$$Cu_2O + H_2O + 2e^- \rightleftharpoons 2Cu + 2OH^- \quad (1)$$

$$2CuO + H_2O + 2e^- \rightleftharpoons Cu_2O + 2OH^- \quad (2)$$

The potentials for both of these reactions are pH-dependent.[59] For the 5 M NaOH solution used in these experiments (pH = 14.7), the electrode potentials for these half-reactions are −0.6 V vs Ag/AgCl for reaction 1 and −0.4 V vs Ag/AgCl for reaction 2. Based on the Pourbaix diagram for Cu,[59] CuO will dissolve in 5 M NaOH (pH = 14.7) via the following reaction:

$$CuO + H_2O + 2OH^- \rightarrow [Cu(OH)_4]^{2-} \quad (3)$$

Based on XPS, both surface oxidation and reduction of the Cu_2O microcrystals occur when the microcrystals are immersed in 5 M NaOH (Figure 3, Figures S10 and S11). As shown in Figure 7, these processes are both enhanced under illumination but at different potential windows. At more positive potentials, illumination produces an anodic current, while illumination enhances the cathodic current at more negative potentials. The absorption of photons with energies above the band gap of Cu_2O creates photoexcited electron−hole pairs. Photogenerated electrons in the conduction band can reduce Cu_2O either directly via reaction 1 or through the redeposition of copper ions that have dissolved in the NaOH solution. Two observations suggest the direct reduction of Cu_2O occurs at the surface of the microcrystals: (1) Cu deposition was not found on the exposed regions of the Au substrate as measured by energy dispersive spectroscopy. (2) As noted above, adding $Cu(NO_3)_2$ to the deposition solution does not alter the formation of the hollow Cu nanoshells (Figure S14). Photogenerated holes in the valence band can oxidize Cu_2O via reaction 2, leading to the dissolution of $[Cu(OH)_4]^{2-}$ ions via reaction 3. As described in the next section, the initial electrochemical potential of the Cu_2O microcrystals in combination with the applied potential controls whether electrons or holes are driven to the semiconductor/liquid interface. Even though the measured current is cathodic at potentials of −0.8 and −1.0 V vs Ag/AgCl (Figure 7c,d), etching of the {111} facets still occurs as shown in Figure 6c,d. In these cases, oxygen can serve as the oxidant to etch the microcrystals via the following reactions:[38,39]

$$2Cu_2O + \frac{1}{2}O_2 + 3H_2O + 2OH^- \rightarrow 4Cu(OH)_2 \quad (4)$$

DOI: 10.1021/acs.chemmater.9b02240
Chem. Mater. 2019, 31, 8000−8011

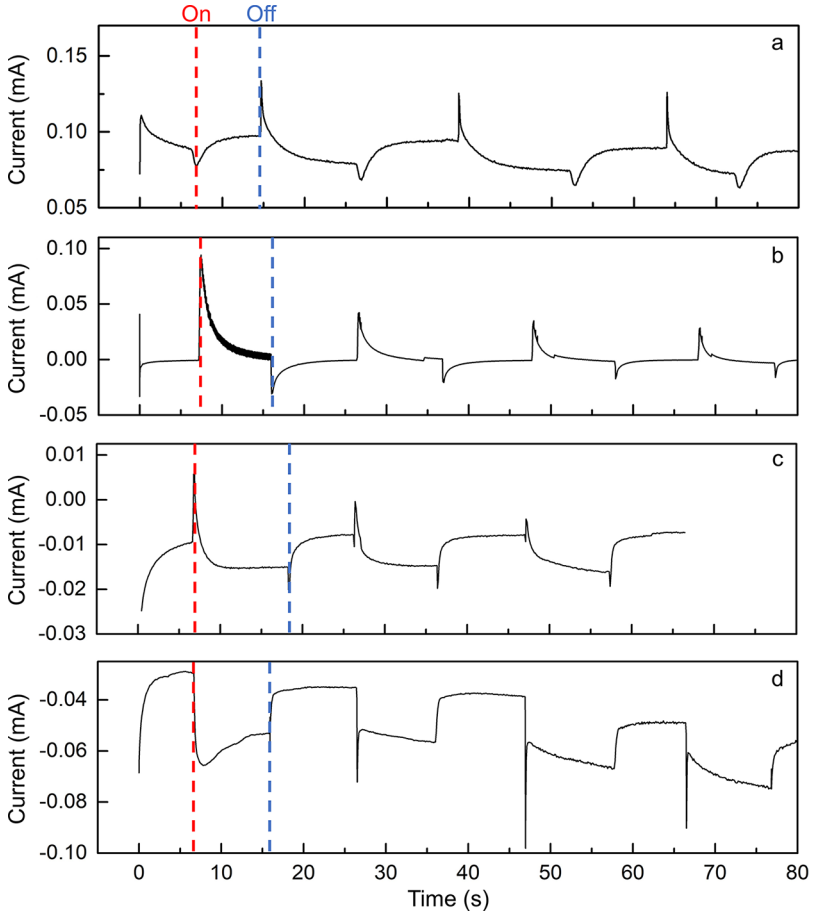

Figure 7. Current vs time traces for Cu_2O microcrystals while the illumination from an ELH lamp was switched on and off at applied potentials of (a) $E = -0.3$ V, (b) $E = -0.5$ V, (c) $E = -0.8$ V, and (d) $E = -1.0$ V vs Ag/AgCl in 5 M NaOH. The dashed red and blue lines show examples of when the lamp was turned on and off, respectively.

$$Cu(OH)_2 + 2OH^- \rightarrow [Cu(OH)_4]^{2-} \quad (5)$$

Correspondingly, we observed slower etching of the {111} facets at −1.0 V vs Ag/AgCl when the concentration of NaOH was decreased to 2.5 or 1 M (Figures S15 and S16).

Energetics of the Semiconductor/Liquid Interface. Figure 8a shows the alignment of the electronic band edge potentials for Cu_2O with the electrode potentials for reactions 1 and 2 that control the reduction and oxidation of Cu_2O (the energies of the conduction and valence band edges are divided by the charge of an electron to convert them to potentials). This alignment is based on a previous report by Kelly and co-workers for electrodeposited Cu_2O films.[60] As has been previously demonstrated for metal oxide semiconductors, we also assume that both the conduction and valence band levels of Cu_2O move 59 mV per pH unit.[61,62] Thus, the relative differences between the electrode potentials in reactions 1 and 2 and the band edge positions of Cu_2O do not change with pH. We performed electrochemical impedance spectroscopy (EIS) to measure the flat-band potential of the semiconductor microcrystals and determine the initial position of the Fermi level for Cu_2O before contact with the solution. Mott−Schottky plots ($1/C^2$ vs applied potential where C is the space-charge capacitance measured from EIS) at different frequencies are provided in Figure S22. The x-intercepts for these plots give the flat-band potential, which has a value between −0.60 and −0.65 V vs Ag/AgCl for frequencies ranging from 5 to 75 kHz. The average value of −0.63 V vs Ag/AgCl indicates that our Cu_2O microcrystals are slightly n-type with the Fermi level closer to the conduction band edge (Figure 8a). While Cu_2O is often p-type due to the presence of native copper ion vacancies, dendritic Cu_2O films electrodeposited under similar conditions to our samples were also found to be n-type with a flat-band potential of −0.78 V vs Ag/AgCl.[51] Our measured value of the flat-band potential also agrees with the photocurrent measurements shown in Figure S21 where there is a crossover between illumination making the current more positive and it making the current more negative in between −0.60 and −0.65 V vs Ag/AgCl.

As the initial Fermi level position for Cu_2O is more negative (i.e., closer to the vacuum level) than the electrode potential for either redox couple, upward bending of the conduction and valence bands occurs at open circuit (Figure 8b). Thus, in the absence of an applied potential photogenerated hole carriers will be driven to the semiconductor/liquid interface leading to oxidative etching of the microcrystals as observed in Figures S18 and S20. As the applied potential is made more negative, the degree of band bending will decrease (Figure 8c). Under these conditions, the dark current will be cathodic as observed in Figure 7b. However, under illumination photogenerated holes will still be driven to the semiconductor/liquid interface, leading to an anodic photocurrent contribution (i.e., oxidation of Cu^+) as seen in Figure 7b and enhanced etching of the microcrystals as observed in Figure 6a,b. Once the applied potential is more negative than the flat-band potential, the

DOI: 10.1021/acs.chemmater.9b02240
Chem. Mater. 2019, 31, 8000−8011

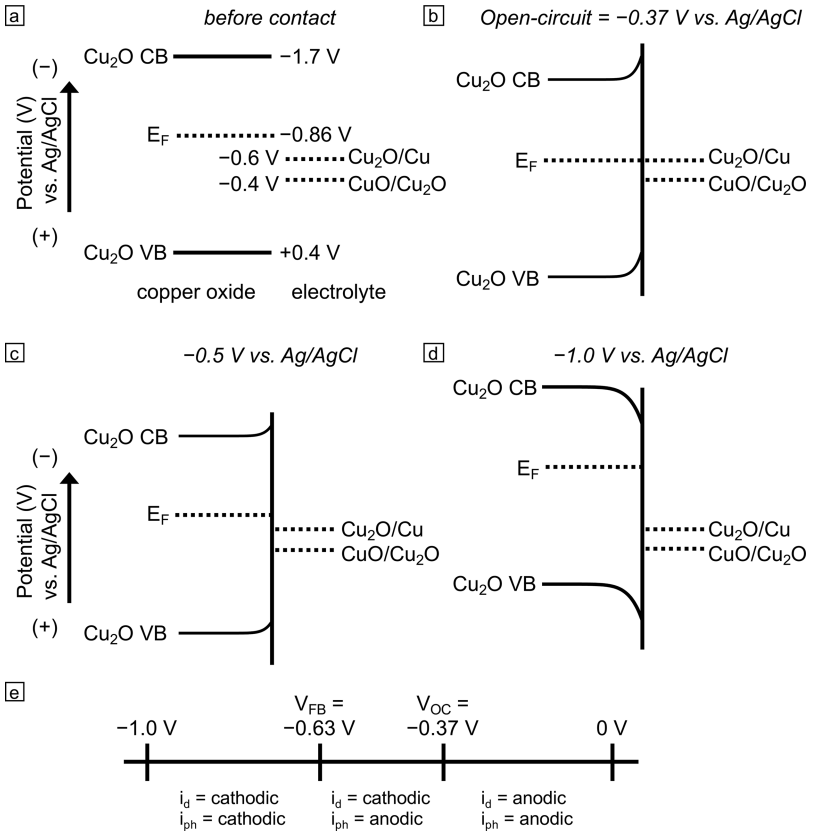

Figure 8. Energy level diagrams showing band bending at the semiconductor/liquid interface at different applied potentials. (a) Alignment of the conduction and valence bands of Cu_2O with the electrode potentials that control the oxidation and reduction of Cu_2O. (b) Equilibration of the Fermi level of Cu_2O with either redox couple leads to upward band bending of the conduction and valence bands at the semiconductor/liquid interface such that photogenerated holes in the valence band of Cu_2O will migrate to the surface. (c) A negative bias will reduce the degree of band bending and (d) lead to downward band bending at a bias greater than the flat-band potential such that photogenerated electrons in the conduction band will migrate to the surface. (e) Summary of the dark current (i_d) and photocurrent (i_{ph}) contributions at different potential windows. V_{OC} = the open-circuit potential, and V_{FB} = the flat-band potential. All potential values are referenced to Ag/AgCl.

band bending in Cu_2O reverses such that holes are depleted at the semiconductor/liquid interface. Thus, at more negative potentials (E = −0.8 and −1.0 V vs Ag/AgCl), photogenerated electrons are driven to the surface, leading to the observed cathodic current that is enhanced under illumination (Figure 7c,d). Correspondingly, at these potentials the reduction of copper ions leads to formation of the Cu shell as observed in Figure 6c,d, while etching at {111} facets occurs via reactions 4 and 5 (using O_2 as the oxidant rather than photogenerated holes). Once Cu metal has grown on the {111} facets, further extraction of photogenerated charges will be controlled by the energetics of the Cu_2O/Cu interface. Based on the work function of polycrystalline Cu near 4.5 eV vs vacuum (giving a potential of −0.2 V vs Ag/AgCl),[63] photogenerated electrons will still be driven to the surface of the microcrystals over the potential range in which we observe growth of the Cu nanoshells.

Figure 8e summarizes the expected currents in the dark and under illumination at different potential windows based on the model described above. This model matches the observed photocurrents shown in Figure 7 and Figure S21. At a bias that is more positive than the open-circuit potential the dark current is anodic. At a bias that is in between the open-circuit and flat-band potentials, the dark current is cathodic, corresponding to reduction of the Cu_2O microcrystals. However, under illumination the combination of photogenerated holes and surface-adsorbed hydroxide ions leads to oxidative etching of the {100} facets via reactions 2 and 3. At potentials more negative than the flat-band potential, illumination drives electrons to the surface to reduce Cu^+ ions at {100} facets according to reaction 1. Changes in the surface area of the Cu_2O microcrystals during the transformation as well as dopant density (as Cu^0 is an n-type dopant in Cu_2O) will also affect the resulting current density. However, it is difficult to disentangle the relative contributions of these simultaneous changes as both the dopant density and electrochemical surface area appear in the denominator of the Mott−Schottky equation used to determine the flat-band potential.

Facet Selectivity of Photoelectrochemical Reactions on Cu_2O. The schematic in Figure 8 does not include the effect of surface structure on the degree of band bending at the semiconductor/liquid interface. Different structures for {100} and {111} facets interfaced with vacuum have been determined by using density functional theory.[35,36,41,64,65] Generally, the {100} surface is terminated with coordinatively unsaturated oxygen while the {111} surface contains both coordinatively unsaturated Cu and O atoms. These different surface terminations affect the electric dipole at the semiconductor/liquid interface and lead to different degrees of band bending.[66]

DOI: 10.1021/acs.chemmater.9b02240
Chem. Mater. 2019, 31, 8000−8011

We attribute the light-driven growth of a Cu shell on the {100} facets at more negative potentials (Figure 7c,d) to the selective extraction of photogenerated electrons from these surfaces. Facet-selective extraction of photogenerated charge carriers has been observed in other semiconductor microcrystals including $BiVO_4$ and TiO_2.[67−69] While there is some debate in the current literature,[32,33] several reports have used DFT calculations to show that the potential of the valence band for the {100} surface of Cu_2O is more positive (further from the vacuum level) compared to the {111} surface, creating a potential barrier for photogenerated holes.[34,35] This hole-blocking layer will lead to selective extraction of photogenerated electrons from {100} facets. As discussed further below, both experiment and theory indicate that O_2 and OH^- bind more strongly to the {100} facets of Cu_2O. However, once the Cu layer has formed on the {100} facets, they are protected from chemical etching, while the exposed {111} facets under these conditions are slowly etched via reactions 4 and 5.

Oxidative photoetching of the Cu_2O {100} facets via reactions 2 and 3 as observed in Figure 6 at applied potentials more positive than the flat-band potential requires both photogenerated holes at the surface and the adsorption of hydroxide anions. Note that these surface reactions do not involve O_2 like the oxidative etching of {111} facets observed at more negative potentials via reactions 4 and 5. Thus, while the exclusion of O_2 by purging the solution with Ar did inhibit growth of the hollow nanoshells at −1.0 V vs Ag/AgCl (Figure S17), it did not have a noticeable effect on the selective photoetching of {100} facets in the absence of an applied potential (Figures S18). The light-driven etching of {100} facets at more positive potentials (Figure 6a,b) could arise from the selective extraction of photogenerated holes from the {100} facets. This mechanism would require a potential-dependent change in the relative positions of the electronic energy levels for the {100} and {111} facets such that holes are selectively extracted from {100} facets at more positive potentials, while electrons are selectively extracted from {100} facets at more negative potentials. The applied potential would control restructuring of the {100} and {111} facets and change the relative degree of band bending at the semiconductor/liquid interface. Restructuring of copper and copper oxide surfaces under an applied potential has been observed by scanning tunneling microscopy.[70−72] This mechanism could explain debate in the literature as to whether {100} facets provide a potential barrier for electrons or holes.[32−35] The potential-dependent surface structure of the {100} and {111} facets would determine which carrier is preferentially extracted from which facet.

While we cannot rule out the mechanism above, we propose the facet-selective etching of {100} facets is due to selective adsorption of hydroxide ions on the {100} facets. The adsorption of OH^- is needed in the oxidative dissolution of Cu_2O to $[Cu(OH)_4]^{2-}$. Both X-ray photoelectron spectroscopy and DFT calculations on single crystal Cu_2O surfaces indicate that H_2O and OH^- as well as other oxygen-containing species including O_2, CO_2, and glucose bind more strongly to the Cu_2O {100} surface than the {111} surface.[36,46,73−77] Structures similar to those observed in Figure 6 and Figure S20 (with the {100} facets etched) have been observed through oxidative etching in the dark.[30,42,78] We also observed slow etching of the {100} facets when the microcrystals were immersed in NaOH in the dark (see Figure S19), but the process was significantly slower compared to when the microcrystals were illuminated.

CONCLUSIONS

Hollow Cu nanoshells and Cu_2O/Cu core/shell heterostructures have been synthesized through the transformation of faceted Cu_2O microcrystals using illumination and an applied bias. Light mediates the deposition of copper metal on the {100} facets due to selective extraction of photogenerated electrons from these surfaces. This process only occurs when the applied potential is sufficiently negative to produce downward band bending at the semiconductor/liquid interface. The formation of the hollow structures can be controlled by tuning the reaction time, intensity and wavelength of the incident light, and the electrolyte concentration. While the focus of this work was the growth mechanism of these novel structures, hollow metal nanoshells have applications in electrocatalysis[79,80] and in chemical sensing via surface-enhanced Raman scattering.[81,82]

EXPERIMENTAL SECTION

Materials. All chemicals were used as received. Copper nitrate trihydrate ($Cu(NO_3)_2·3H_2O$, ≥99%), copper sulfate pentahydrate ($CuSO_4·5H_2O$, ≥98%), sodium hydroxide (NaOH, ≥97%), sodium citrate tribasic dihydrate (≥99%), sodium carbonate (Na_2CO_3, ≥99.95%), sodium dodecyl sulfate (SDS, ≥99%), nitric acid (HNO_3, ≥97%), sodium chloride (NaCl, ≥99%), ethylenediamine, and polyvinylpyrrolidone (PVP) with an average molecular weight of 40000 were purchased from Sigma-Aldrich. Ethanol (200 proof, 100%) was purchased from Fisher Scientific. D-(+)-glucose (≥99%), platinum gauze (Pt, 100 mesh, 99.9% metals basis), and Pt wire (0.5 mm diameter, 99.95% metals basis) were purchased from Alfa Aesar. Chrome-plated tungsten rods and gold pellets (99.999%) for metal evaporation were purchased from Kurt J. Lesker. All aqueous solutions were made by using purified water from a GenPure Pro water purification system with at least 17.30 MΩ·cm resistivity.

Preparation of Electrodes. The counter electrode consisted of Pt gauze attached to a Pt wire. The Pt wire was soldered to a Sn−Cu wire, and the soldered joint was sealed in a glass tube. For the working electrodes, 100 Å of chromium followed by 500 Å of gold was deposited onto glass slides by using an Edwards Auto 306 thermal evaporator with a base pressure below 10^{-7} Torr. Each working electrode was rinsed with purified water and then dried with nitrogen gas before use. A silver/silver chloride (Ag/AgCl) electrode in 3 M NaCl was used as the reference electrode.

Electrodeposition of Cuprous Oxide (Cu_2O) Microcrystals. Cu_2O microcrystals were electrodeposited from an aqueous solution of 0.02 M $Cu(NO_3)_2$ based on a previous report with some modifications.[26] SDS and NaCl were added to the solution in some cases to control the morphology of the microcrystals (see Table S1). Before electrodeposition, the pH of the solution was adjusted to 4.1 through the dropwise addition of 0.1 M HNO_3. If the solution contained SDS, the pH was adjusted before SDS was added because the surfactant prevented a reliable pH reading.

A custom electrochemical cell was used for all electrodeposition experiments. The cell was made from borosilicate glass with openings at the top for the electrodes and a flat window on the side for illumination (used only in the photoinduced transformations described below). The electrochemical cell was partially immersed in a water bath set on a hot plate. A temperature probe was inserted into the electrochemical cell to control the temperature. The electrolyte solution was heated and kept at 60 °C during the electrodeposition of all Cu_2O samples.

A BioLogic VSP-300 potentiostat/galvanostat was used to perform all electrochemical and photoelectrochemical experiments. To grow different shapes of Cu_2O microcrystals, the deposition solution contained 0.17 M SDS and 0.005 M NaCl in some cases (see Table

DOI: 10.1021/acs.chemmater.9b02240
Chem. Mater. 2019, 31, 8000−8011

S1). Either a constant current or a pulsed current was used to electrodeposit the microcrystals. A photo scanner was used to scan images of the working electrodes, and their areas were measured by using ImageJ software. Table S1 provides the current waveform used for each sample and the total deposition time.

Synthesis of Colloidal Cu_2O Microcrystals. The colloidal Cu_2O microcrystals shown in Figures S19 and S20 were synthesized by using a previously reported procedure.[83] First, an aqueous solution was made by mixing 17 mL of water, 1 mL of 0.68 M $CuSO_4$, and 1.2 g of PVP (M_W = 40000) in a round-bottom flask. The solution was stirred by using a magnetic stir bar for 15−20 min, and then 1 mL of an aqueous solution containing 0.74 M sodium citrate and 1.2 M Na_2CO_3 solution was added dropwise to the $CuSO_4$ solution. Upon this addition, the solution began to turn dark blue. After 10 min, 1 mL of an aqueous solution containing 1.4 M glucose was added dropwise to the $CuSO_4$ solution. The solution was kept in a water bath at 80 °C for 2 h and then cooled to room temperature. The brick-red precipitate was collected by centrifuging the mixture at 8000 rpm for 4 min. The supernatant was removed, and 10 mL of purified water was added to the precipitate. The process of centrifugation, removal of the supernatant, and redispersion in fresh solvent was repeated two more times. For the last two cycles, 10 mL of ethanol was used instead of water. The final dispersion in ethanol was transferred to a glass vial for further use. For the photoinduced transformations described below, the colloidal Cu_2O microcrystals were first sonicated to redisperse them into solution. A drop of this suspension was then diluted with 2 mL of ethanol and drop-cast onto a Si(111) substrate.

Photoinduced Transformation of Cu_2O Microcrystals. A broadband, ELH-type light bulb was used as the illumination source for most experiments. The irradiance was measured by using a calibrated Si photodiode from ThorLabs (FDS-100 CAL). Before the transformation the photodiode was placed at the same location in the electrochemical cell as the working electrode (facing the optical window of the electrochemical cell), and the current was measured under illumination with the ELH lamp. A typical current reading was 0.02 A, which based on the wavelength-dependent responsivity and active area (3.6 × 3.6 mm^2) of the photodiode gives an irradiance of 567 mW/cm^2. High-power, light-emitting diodes (LEDs) with peak wavelengths of 455 and 625 nm and full widths at half-maxima of ∼30 nm were used in some experiments instead of the ELH lamp (see Table S2). Similar to the electrodeposition of the Cu_2O microcrystals, Pt gauze was used as the counter electrode and Ag/AgCl was used as the reference electrode. The electrodeposited Cu_2O microcrystals on Au substrates were used as the working electrode and immersed in a solution of NaOH (typically 5 M). The applied potential used to form the hollow Cu shells was typically −1.0 V vs Ag/AgCl. The times held at this potential under illumination for different samples are provided in Table S2. Other applied potentials and concentrations of NaOH were used for some samples. The parameters used to prepare different samples are provided in Table S2. In some cases, no bias was applied (labeled as open circuit in Table S2).

Characterization. Cyclic voltammetry (CV) was performed to characterize the potentials for different redox reactions to occur on the Au substrate and Cu_2O microcrystals. All CV scans started at open circuit. For each scan, the potential was first swept in the positive direction to +0.2 V vs Ag/AgCl, then swept in the negative direction to −1.2 V, and finally swept back to +0.2 V. The scan rate was 20 mV/s, and two consecutive CV scans were performed for each electrode. In some cases, the solution was purged with argon for 30 min. Otherwise, the electrochemical cell was left open to air.

Electrochemical impedance spectroscopy (EIS) was performed to determine the flat-band potential of the as-synthesized Cu_2O microcrystals on Au substrates in a solution of 0.1 M NaOH. The frequencies scanned were 5 to 75 kHz. The ac potential oscillation was 10 mV, and the dc potential range was −0.2 to −0.6 V vs Ag/AgCl. A circuit consisting of two resistors (R_1 and R_2), a capacitor (C_2), and a restricted diffusion element (M_2): $[R_1 + C_2/(R_2 + M_2)]$ was used to model the electrochemical cell based on fits to Nyquist plots at different applied potentials. Mott−Schottky plots ($1/C_2^2$ vs the applied potential where C_2 is the space-charge capacitance) were extracted from EIS data. The x-intercepts determined from linear fits to these plots give the flat-band potential, which varied from −0.60 to −0.65 V vs Ag/AgCl for different frequencies (see Table S3).

Scanning electron microscopy (SEM) images were collected by using a JEOL 7001LVF field emission scanning electron microscope operated at an acceleration voltage of 15 kV. After electrodeposition, the working electrode was cut to approximately 1 × 1 cm^2 pieces, and the conductive top surface of the substrate was connected with copper tape to the SEM sample holder to avoid charge buildup. The SEM was equipped with an Oxford Aztec live x-max energy dispersive X-ray spectroscopy (EDXS) system, and EDXS spectra were collected at an acceleration voltage of 15 kV.

X-ray diffraction (XRD) patterns were collected by using a Bruker D8 Advance X-ray diffractometer (Cu Kα = 0.15418 nm). The step size for the XRD measurements was 0.02° in 2θ, and the scan rate was 0.5 s per step. To prepare samples for XRD, the working electrode was cut to approximately 1 × 1 cm^2 pieces and placed onto a zero-background, silicon diffraction plate (MTI Corporation).

X-ray photoelectron spectroscopy (XPS) was performed by using a Physical Electronics 5000 VersaProbe II Scanning ESCA (XPS) Microprobe system with a base pressure below 1 × 10^{-9} Torr. XPS data were acquired by using the 1486.6 eV line from a monochromated Al Kα source at 150 W with a multichannel detector set to a pass energy of 23.5 eV for the high-resolution scans. The peak fitting was processed by using XPSPEAK software with a Shirley background. The kinetic energies of the Auger spectra were calculated by subtracting the binding energies from the X-ray source energy (1486.6 eV). The assignments of peaks in the photoelectron spectra of copper and oxygen and the Auger spectra of copper were based on previous literature.[36,54,55,84]

Absorption spectra of solid samples were acquired by diffuse reflectance by using a Cary 5000 spectrometer equipped with a 150 mm integrating sphere. A PMT detector was used for ultraviolet (UV) and visible wavelengths (250−800 nm), and a lead sulfide detector was used for near-infrared (NIR) wavelengths (800−1200 nm). A tungsten halogen lamp was used as the source for visible and NIR wavelengths (350−1200 nm), and a deuterium lamp was used for the UV region (250−350 nm). The scan rate for each measurement was 600 nm/min, and the step size was 1.0 nm. The absorbance spectrum of a bare Au film was subtracted from the sample spectra of the Cu_2O microcrystals electrodeposited on Au. The absorption spectra of solutions of $Cu(NO_3)_2$ and NaOH were measured with a Cary 60 spectrometer.

■ ASSOCIATED CONTENT

Supporting Information

The Supporting Information is available free of charge on the ACS Publications website at DOI: 10.1021/acs.chemmater.9b02240.

Supporting tables providing the conditions used to prepare different samples of the Cu_2O microcrystals and hollow Cu nanoshells, cyclic voltammograms of the Au substrates and Cu_2O microcrystals, current traces during the transformation of Cu_2O microcrystals in the dark and under illumination, SEM images of Cu_2O microcrystals transformed in the dark at higher current densities, absorption spectrum of Cu_2O microcrystals, SEM images of Cu_2O microcrystals transformed under different light intensities and wavelengths, additional XRD patterns and XPS of Cu_2O microcrystals transformed under different potentials and illumination conditions, cyclic voltammogram and absorption spectrum of the NaOH solution used to transform the Cu_2O microcrystals, SEM images of Cu_2O microcrystals transformed with $Cu(NO_3)_2$ added to the electrolyte solution, SEM images and XRD pattern of Cu_2O microcrystals transformed using lower concentrations

DOI: 10.1021/acs.chemmater.9b02240
Chem. Mater. 2019, 31, 8000−8011

of NaOH, SEM images of Cu_2O microcrystals transformed using solutions purged with Ar and O_2, SEM images of Cu_2O microcrystals etched in NaOH in the dark, SEM images of Cu_2O microcrystals transformed without an applied bias, photocurrent traces for Cu_2O microcrystals at different applied potentials, Mott–Schottky plots at different frequencies, supporting table of flat-band potentials measured at different frequencies (PDF)

AUTHOR INFORMATION

Corresponding Author

*E-mail: sadtler@wustl.edu.

ORCID

Bryce Sadtler: 0000-0003-4860-501X

Notes

The authors declare no competing financial interest.

ACKNOWLEDGMENTS

This material is based upon work supported by the National Science Foundation under CHE-1753344. Electron microscopy and X-ray photoelectron spectroscopy were performed at the Institute of Materials Science & Engineering at Washington University. X-ray diffraction was performed in the Department of Earth and Planetary Sciences at Washington University. B.M.C. acknowledges support from the uSTAR Summer Scholars Program at Washington University. T.Z. acknowledges support from the STARS summer research program at the University of Missouri-St. Louis.

REFERENCES

(1) Tan, M. X.; Laibinis, P. E.; Nguyen, S. T.; Kesselman, J. M.; Stanton, C. E.; Lewis, N. S. Principles and Applications of Semiconductor Photoelectrochemistry. *Prog. Inorg. Chem.* **2007**, *41*, 21–144.

(2) Walter, M. G.; Warren, E. L.; McKone, J. R.; Boettcher, S. W.; Mi, Q.; Santori, E. A.; Lewis, N. S. Solar Water Splitting Cells. *Chem. Rev.* **2010**, *110*, 6446–6473.

(3) Warren, S. C.; Thimsen, E. Plasmonic Solar Water Splitting. *Energy Environ. Sci.* **2012**, *5*, 5133–5146.

(4) Tan, C.; Qin, C.; Sadtler, B. Light-Directed Growth of Metal and Semiconductor Nanostructures. *J. Mater. Chem. C* **2017**, *5*, 5628–5642.

(5) Langille, M. R.; Personick, M. L.; Mirkin, C. A. Plasmon-Mediated Syntheses of Metallic Nanostructures. *Angew. Chem., Int. Ed.* **2013**, *52*, 13910–13940.

(6) Jin, R.; Cao, Y.; Mirkin, C. A.; Kelly, K. L.; Schatz, G. C.; Zheng, J. G. Photoinduced Conversion of Silver Nanospheres to Nanoprisms. *Science* **2001**, *294*, 1901–1903.

(7) Zhang, J.; Langille, M. R.; Mirkin, C. A. Synthesis of Silver Nanorods by Low Energy Excitation of Spherical Plasmonic Seeds. *Nano Lett.* **2011**, *11*, 2495–2498.

(8) Personick, M. L.; Langille, M. R.; Zhang, J.; Wu, J.; Li, S.; Mirkin, C. A. Plasmon-Mediated Synthesis of Silver Cubes with Unusual Twinning Structures Using Short Wavelength Excitation. *Small* **2013**, *9*, 1947–1953.

(9) Zhai, Y.; DuChene, J. S.; Wang, Y.-C.; Qiu, J.; Johnston-Peck, A. C.; You, B.; Guo, W.; DiCiaccio, B.; Qian, K.; Zhao, E. W.; Ooi, F.; Hu, D.; Su, D.; Stach, E. A.; Zhu, Z.; Wei, W. D. Polyvinylpyrrolidone-Induced Anisotropic Growth of Gold Nanoprisms in Plasmon-Driven Synthesis. *Nat. Mater.* **2016**, *15*, 889–895.

(10) Xue, C.; Métraux, G. S.; Millstone, J. E.; Mirkin, C. A. Mechanistic Study of Photomediated Triangular Silver Nanoprism Growth. *J. Am. Chem. Soc.* **2008**, *130*, 8337–8344.

(11) Wu, X.; Redmond, P. L.; Liu, H.; Chen, Y.; Steigerwald, M.; Brus, L. Photovoltage Mechanism for Room Light Conversion of Citrate Stabilized Silver Nanocrystal Seeds to Large Nanoprisms. *J. Am. Chem. Soc.* **2008**, *130*, 9500–9506.

(12) Thrall, E. S.; Preska Steinberg, A.; Wu, X.; Brus, L. E. The Role of Photon Energy and Semiconductor Substrate in the Plasmon-Mediated Photooxidation of Citrate by Silver Nanoparticles. *J. Phys. Chem. C* **2013**, *117*, 26238–26247.

(13) Jin, R.; Charles Cao, Y.; Hao, E.; Metraux, G. S.; Schatz, G. C.; Mirkin, C. A. Controlling Anisotropic Nanoparticle Growth through Plasmon Excitation. *Nature* **2003**, *425*, 487–490.

(14) Maillard, M.; Huang, P.; Brus, L. Silver Nanodisk Growth by Surface Plasmon Enhanced Photoreduction of Adsorbed [Ag^+]. *Nano Lett.* **2003**, *3*, 1611–1615.

(15) Sadtler, B.; Burgos, S. P.; Batara, N. A.; Beardslee, J. A.; Atwater, H. A.; Lewis, N. S. Phototropic Growth Control of Nanoscale Pattern Formation in Photoelectrodeposited Se-Te Films. *Proc. Natl. Acad. Sci. U. S. A.* **2013**, *110*, 19707–19712.

(16) Carim, A. I.; Batara, N. A.; Premkumar, A.; Atwater, H. A.; Lewis, N. S. Self-Optimizing Photoelectrochemical Growth of Nanopatterned Se-Te Films in Response to the Spectral Distribution of Incident Illumination. *Nano Lett.* **2015**, *15*, 7071–7076.

(17) Carim, A. I.; Batara, N. A.; Premkumar, A.; Atwater, H. A.; Lewis, N. S. Polarization Control of Morphological Pattern Orientation During Light-Mediated Synthesis of Nanostructured Se-Te Films. *ACS Nano* **2016**, *10*, 102–111.

(18) Carim, A. I.; Batara, N. A.; Premkumar, A.; May, R.; Atwater, H. A.; Lewis, N. S. Morphological Expression of the Coherence and Relative Phase of Optical Inputs to the Photoelectrodeposition of Nanopatterned Se-Te Films. *Nano Lett.* **2016**, *16*, 2963–2968.

(19) Carim, A. I.; Hamann, K. R.; Batara, N. A.; Thompson, J. R.; Atwater, H. A.; Lewis, N. S. Template-Free Synthesis of Periodic Three-Dimensional PbSe Nanostructures Via Photoelectrodeposition. *J. Am. Chem. Soc.* **2018**, *140*, 6536–6539.

(20) Simonoff, E.; Lichterman, M. F.; Papadantonakis, K. M.; Lewis, N. S. Influence of Substrates on the Long-Range Order of Photoelectrodeposited Se-Te Nanostructures. *Nano Lett.* **2019**, *19*, 1295–1300.

(21) Scharfe, M. E.; Tabak, M. D. Bulk Space Charge and Transient Photoconductivity in Amorphous Selenium. *J. Appl. Phys.* **1969**, *40*, 3230–3237.

(22) Vaezi-Nejad, S. M.; Juhasz, C. Effect of Chlorine on Xerographic Properties of a-Se:Te Alloys. *J. Mater. Sci.* **1988**, *23*, 3286–3289.

(23) Kim, G. I.; Shirafuji, J.; Inuishi, Y. Transport of Photoexcited Carriers in Evaporated Ge_xSe_{1-x} Glass Films. *Jpn. J. Appl. Phys.* **1981**, *20*, 1377–1383.

(24) Zheng, X.; Zhao, X.; Guo, D.; Tang, B.; Xu, S.; Zhao, B.; Xu, W.; Lombardi, J. R. Photochemical Formation of Silver Nanodecahedra: Structural Selection by the Excitation Wavelength. *Langmuir* **2009**, *25*, 3802–3807.

(25) Golden, T. D.; Shumsky, M. G.; Zhou, Y.; VanderWerf, R. A.; Van Leeuwen, R. A.; Switzer, J. A. Electrochemical Deposition of Copper(I) Oxide Films. *Chem. Mater.* **1996**, *8*, 2499–2504.

(26) Siegfried, M. J.; Choi, K.-S. Electrochemical Crystallization of Cuprous Oxide with Systematic Shape Evolution. *Adv. Mater.* **2004**, *16*, 1743–1746.

(27) Siegfried, M. J.; Choi, K.-S. Directing the Architecture of Cuprous Oxide Crystals During Electrochemical Growth. *Angew. Chem., Int. Ed.* **2005**, *44*, 3218–3223.

(28) Choi, K.-S. Shape Control of Inorganic Materials Via Electrodeposition. *Dalton Transactions* **2008**, 5432–5438.

(29) Zhang, Y.; Deng, B.; Zhang, T.; Gao, D.; Xu, A.-W. Shape Effects of Cu_2O Polyhedral Microcrystals on Photocatalytic Activity. *J. Phys. Chem. C* **2010**, *114*, 5073–5079.

(30) Xu, Y.; Wang, H.; Yu, Y.; Tian, L.; Zhao, W.; Zhang, B. Cu_2O Nanocrystals: Surfactant-Free Room-Temperature Morphology-Modulated Synthesis and Shape-Dependent Heterogeneous Organic Catalytic Activities. *J. Phys. Chem. C* **2011**, *115*, 15288–15296.

DOI: 10.1021/acs.chemmater.9b02240
Chem. Mater. 2019, 31, 8000–8011

(31) Li, L.; Nan, C.; Peng, Q.; Li, Y. Selective Synthesis of Cu_2O Nanocrystals as Shape-Dependent Catalysts for Oxidative Arylation of Phenylacetylene. *Chem. - Eur. J.* **2012**, *18*, 10491−10496.
(32) Yuan, G.-Z.; Hsia, C.-F.; Lin, Z.-W.; Chiang, C.; Chiang, Y.-W.; Huang, M. H. Highly Facet-Dependent Photocatalytic Properties of Cu_2O Crystals Established through the Formation of Au-Decorated Cu_2O Heterostructures. *Chem. - Eur. J.* **2016**, *22*, 12548−12556.
(33) Zheng, Z.; Huang, B.; Wang, Z.; Guo, M.; Qin, X.; Zhang, X.; Wang, P.; Dai, Y. Crystal Faces of Cu_2O and Their Stabilities in Photocatalytic Reactions. *J. Phys. Chem. C* **2009**, *113*, 14448−14453.
(34) Wang, L.; Ge, J.; Wang, A.; Deng, M.; Wang, X.; Bai, S.; Li, R.; Jiang, J.; Zhang, Q.; Luo, Y.; Xiong, Y. Designing p-Type Semiconductor-Metal Hybrid Structures for Improved Photocatalysis. *Angew. Chem., Int. Ed.* **2014**, *53*, 5107−5111.
(35) Su, Y.; Li, H.; Ma, H.; Robertson, J.; Nathan, A. Controlling Surface Termination and Facet Orientation in Cu_2O Nanoparticles for High Photocatalytic Activity: A Combined Experimental and Density Functional Theory Study. *ACS Appl. Mater. Interfaces* **2017**, *9*, 8100−8106.
(36) Zhang, X.; Zhang, Y.; Huang, H.; Cai, J.; Ding, K.; Lin, S. Electrochemical Fabrication of Shape-Controlled Cu_2O with Spheres, Octahedrons and Truncated Octahedrons and Their Electrocatalysis for ORR. *New J. Chem.* **2018**, *42*, 458−464.
(37) Hua, Q.; Shang, D.; Zhang, W.; Chen, K.; Chang, S.; Ma, Y.; Jiang, Z.; Yang, J.; Huang, W. Morphological Evolution of Cu_2O Nanocrystals in an Acid Solution: Stability of Different Crystal Planes. *Langmuir* **2011**, *27*, 665−671.
(38) Hua, Q.; Chen, K.; Chang, S.; Ma, Y.; Huang, W. Crystal Plane-Dependent Compositional and Structural Evolution of Uniform Cu_2O Nanocrystals in Aqueous Ammonia Solutions. *J. Phys. Chem. C* **2011**, *115*, 20618−20627.
(39) Pal, J.; Ganguly, M.; Mondal, C.; Roy, A.; Negishi, Y.; Pal, T. Crystal-Plane-Dependent Etching of Cuprous Oxide Nanoparticles of Varied Shapes and Their Application in Visible Light Photocatalysis. *J. Phys. Chem. C* **2013**, *117*, 24640−24653.
(40) Kwon, Y.; Soon, A.; Han, H.; Lee, H. Shape Effects of Cuprous Oxide Particles on Stability in Water and Photocatalytic Water Splitting. *J. Mater. Chem. A* **2015**, *3*, 156−162.
(41) Bao, H.; Zhang, W.; Shang, D.; Hua, Q.; Ma, Y.; Jiang, Z.; Yang, J.; Huang, W. Shape-Dependent Reducibility of Cuprous Oxide Nanocrystals. *J. Phys. Chem. C* **2010**, *114*, 6676−6680.
(42) Sui, Y.; Fu, W.; Zeng, Y.; Yang, H.; Zhang, Y.; Chen, H.; Li, Y.; Li, M.; Zou, G. Synthesis of Cu_2O Nanoframes and Nanocages by Selective Oxidative Etching at Room Temperature. *Angew. Chem., Int. Ed.* **2010**, *49*, 4282−4285.
(43) Liu, X.-W. Selective Growth of Au Nanoparticles on (111) Facets of Cu_2O Microcrystals with an Enhanced Electrocatalytic Property. *Langmuir* **2011**, *27*, 9100−9104.
(44) Zhu, H.; Du, M.; Yu, D.; Wang, Y.; Zou, M.; Xu, C.; Fu, Y. Selective Growth of Au Nanograins on Specific Positions (Tips, Edges and Facets) of Cu_2O Octahedrons to Form Cu_2O-Au Hierarchical Heterostructures. *Dalton Transactions* **2012**, *41*, 13795−13799.
(45) Read, C. G.; Steinmiller, E. M. P.; Choi, K.-S. Atomic Plane-Selective Deposition of Gold Nanoparticles on Metal Oxide Crystals Exploiting Preferential Adsorption of Additives. *J. Am. Chem. Soc.* **2009**, *131*, 12040−12041.
(46) Wang, C.; Tissot, H.; Escudero, C.; Pérez-Dieste, V.; Stacchiola, D.; Weissenrieder, J. Redox Properties of Cu_2O(100) and (111) Surfaces. *J. Phys. Chem. C* **2018**, *122*, 28684−28691.
(47) Alvarez, S.; Ye, S.; Flowers, P. F.; Wiley, B. J. Photocatalytic Growth of Copper Nanowires from Cu_2O Seeds. *Chem. Mater.* **2015**, *27*, 570−573.
(48) Lowe, J. M.; Yan, Q.; Benamara, M.; Coridan, R. H. Direct Photolithographic Patterning of Cuprous Oxide Thin Films Via Photoelectrodeposition. *J. Mater. Chem. A* **2017**, *5*, 21765−21772.
(49) Lowe, J. M.; Coridan, R. H. Mechanistic Control of a Galvanic Replacement Reaction on Cuprous Oxide. *Nanoscale Adv.* **2019**, *1*, 1343−1350.
(50) Giri, S. D.; Sarkar, A. Electrochemical Study of Bulk and Monolayer Copper in Alkaline Solution. *J. Electrochem. Soc.* **2016**, *163*, H252−H259.
(51) McShane, C. M.; Choi, K.-S. Photocurrent Enhancement of n-Type Cu_2O Electrodes Achieved by Controlling Dendritic Branching Growth. *J. Am. Chem. Soc.* **2009**, *131*, 2561−2569.
(52) Switzer, J. A.; Hung, C.-J.; Bohannan, E. W.; Shumsky, M. G.; Golden, T. D.; Van Aken, D. C. Electrodeposition of Quantum-Confined Metal/Semiconductor Nanocomposites. *Adv. Mater.* **1997**, *9*, 334−338.
(53) Switzer, J. A.; Hung, C.-J.; Huang, L.-Y.; Switzer, E. R.; Kammler, D. R.; Golden, T. D.; Bohannan, E. W. Electrochemical Self-Assembly of Copper/Cuprous Oxide Layered Nanostructures. *J. Am. Chem. Soc.* **1998**, *120*, 3530−3531.
(54) Xiang, C.; Kimball, G. M.; Grimm, R. L.; Brunschwig, B. S.; Atwater, H. A.; Lewis, N. S. 820 mV Open-Circuit Voltages from Cu_2O/CH_3CN Junctions. *Energy Environ. Sci.* **2011**, *4*, 1311−1318.
(55) Pike, S. D.; White, E. R.; Regoutz, A.; Sammy, N.; Payne, D. J.; Williams, C. K.; Shaffer, M. S. P. Reversible Redox Cycling of Well-Defined, Ultrasmall Cu/Cu_2O Nanoparticles. *ACS Nano* **2017**, *11*, 2714−2723.
(56) Moore, G. F.; Blakemore, J. D.; Milot, R. L.; Hull, J. F.; Song, H.-e.; Cai, L.; Schmuttenmaer, C. A.; Crabtree, R. H.; Brudvig, G. W. A Visible Light Water-Splitting Cell with a Photoanode Formed by Codeposition of a High-Potential Porphyrin and an Iridium Water-Oxidation Catalyst. *Energy Environ. Sci.* **2011**, *4*, 2389−2392.
(57) Xiang, X.; Fielden, J.; Rodríguez-Córdoba, W.; Huang, Z.; Zhang, N.; Luo, Z.; Musaev, D. G.; Lian, T.; Hill, C. L. Electron Transfer Dynamics in Semiconductor-Chromophore-Polyoxometalate Catalyst Photoanodes. *J. Phys. Chem. C* **2013**, *117*, 918−926.
(58) Swierk, J. R.; McCool, N. S.; Mallouk, T. E. Dynamics of Electron Recombination and Transport in Water-Splitting Dye-Sensitized Photoanodes. *J. Phys. Chem. C* **2015**, *119*, 13858−13867.
(59) Beverskog, B.; Puigdomenech, I. Revised Pourbaix Diagrams for Copper at 25 to 300°C. *J. Electrochem. Soc.* **1997**, *144*, 3476−3483.
(60) de Jongh, P. E.; Vanmaekelbergh, D.; Kelly, J. J. Photoelectrochemistry of Electrodeposited Cu_2O. *J. Electrochem. Soc.* **2000**, *147*, 486−489.
(61) Bolts, J. M.; Wrighton, M. S. Correlation of Photocurrent-Voltage Curves with Flat-Band Potential for Stable Photoelectrodes for the Photoelectrolysis of Water. *J. Phys. Chem.* **1976**, *80*, 2641−2645.
(62) Chen, S.; Wang, L.-W. Thermodynamic Oxidation and Reduction Potentials of Photocatalytic Semiconductors in Aqueous Solution. *Chem. Mater.* **2012**, *24*, 3659−3666.
(63) Anderson, P. A. The Work Function of Copper. *Phys. Rev.* **1949**, *76*, 388−390.
(64) Soon, A.; Todorova, M.; Delley, B.; Stampfl, C. Thermodynamic Stability and Structure of Copper Oxide Surfaces: A First-Principles Investigation. *Phys. Rev. B* **2007**, *75*, 125420-1−9.
(65) Bendavid, L. I.; Carter, E. A. First-Principles Predictions of the Structure, Stability, and Photocatalytic Potential of Cu_2O Surfaces. *J. Phys. Chem. B* **2013**, *117*, 15750−15760.
(66) Choi, K.-S. Shape Effect and Shape Control of Polycrystalline Semiconductor Electrodes for Use in Photoelectrochemical Cells. *J. Phys. Chem. Lett.* **2010**, *1*, 2244−2250.
(67) Ohno, T.; Sarukawa, K.; Matsumura, M. Crystal Faces of Rutile and Anatase TiO_2 Particles and Their Roles in Photocatalytic Reactions. *New J. Chem.* **2002**, *26*, 1167−1170.
(68) Li, R.; Zhang, F.; Wang, D.; Yang, J.; Li, M.; Zhu, J.; Zhou, X.; Han, H.; Li, C. Spatial Separation of Photogenerated Electrons and Holes among {010} and {110} Crystal Facets of $BiVO_4$. *Nat. Commun.* **2013**, *4*, 1432-1−7.
(69) Zhu, W.; Shen, M.; Fan, G.; Yang, A.; Meyer, J. R.; Ou, Y.; Yin, B.; Fortner, J.; Foston, M.; Li, Z.; Zou, Z.; Sadtler, B. Facet-Dependent Enhancement in the Activity of Bismuth Vanadate Microcrystals for the Photocatalytic Conversion of Methane to Methanol. *ACS Applied Nano Materials* **2018**, *1*, 6683−6691.

DOI: 10.1021/acs.chemmater.9b02240
Chem. Mater. 2019, 31, 8000−8011

(70) Matsushima, H.; Taranovskyy, A.; Haak, C.; Gründer, Y.; Magnussen, O. M. Reconstruction of Cu(100) Electrode Surfaces During Hydrogen Evolution. *J. Am. Chem. Soc.* **2009**, *131*, 10362−10363.
(71) Kim, Y.-G.; Baricuatro, J. H.; Javier, A.; Gregoire, J. M.; Soriaga, M. P. The Evolution of the Polycrystalline Copper Surface, First to Cu(111) and Then to Cu(100), at a Fixed CO_2RR Potential: A Study by Operando EC-STM. *Langmuir* **2014**, *30*, 15053−15056.
(72) Tsang, C. F.; Javier, A. C.; Kim, Y.-G.; Baricuatro, J. H.; Cummins, K. D.; Kim, J.; Jerkiewicz, G.; Hemminger, J. C.; Soriaga, M. P. Potential-Dependent Adsorption of CO and Its Low-Overpotential Reduction to CH_3CH_2OH on Cu(511) Surface Reconstructed from Cu(pc): Operando Studies by Seriatim STM-EQCN-DEMS. *J. Electrochem. Soc.* **2018**, *165*, J3350−J3354.
(73) Stenlid, J. H.; Soldemo, M.; Johansson, A. J.; Leygraf, C.; Göthelid, M.; Weissenrieder, J.; Brinck, T. Reactivity at the Cu_2O(100):Cu-H_2O Interface: A Combined DFT and PES Study. *Phys. Chem. Chem. Phys.* **2016**, *18*, 30570−30584.
(74) Nygren, M. A.; Pettersson, L. G. M. H_2O Interaction with the Polar Cu_2O(100) Surface: A Theoretical Study. *J. Phys. Chem.* **1996**, *100*, 1874−1878.
(75) Yu, X.; Zhang, X.; Wang, S.; Feng, G. A Computational Study on Water Adsorption on Cu_2O(111) Surfaces: The Effects of Coverage and Oxygen Defect. *Appl. Surf. Sci.* **2015**, *343*, 33−40.
(76) Mishra, A. K.; Roldan, A.; de Leeuw, N. H. A Density Functional Theory Study of the Adsorption Behaviour of CO_2 on Cu_2O Surfaces. *J. Chem. Phys.* **2016**, *145*, 044709-1−13.
(77) Pastrián, F. A. C.; da Silva, A. G. M.; Dourado, A. H. B.; de Lima Batista, A. P.; de Oliveira-Filho, A. G. S.; Quiroz, J.; de Oliveira, D. C.; Camargo, P. H. C.; Córdoba de Torresi, S. I. Why Could the Nature of Surface Facets Lead to Differences in the Activity and Stability of Cu_2O-Based Electrocatalytic Sensors? *ACS Catal.* **2018**, *8*, 6265−6272.
(78) Lu, C.; Qi, L.; Yang, J.; Wang, X.; Zhang, D.; Xie, J.; Ma, J. One-Pot Synthesis of Octahedral Cu_2O Nanocages Via a Catalytic Solution Route. *Adv. Mater.* **2005**, *17*, 2562−2567.
(79) Chen, C.; Kang, Y.; Huo, Z.; Zhu, Z.; Huang, W.; Xin, H. L.; Snyder, J. D.; Li, D.; Herron, J. A.; Mavrikakis, M.; Chi, M.; More, K. L.; Li, Y.; Markovic, N. M.; Somorjai, G. A.; Yang, P.; Stamenkovic, V. R. Highly Crystalline Multimetallic Nanoframes with Three-Dimensional Electrocatalytic Surfaces. *Science* **2014**, *343*, 1339−1343.
(80) Zhong, X.; Zhang, Y.; Geng, Z.; Shi, F.; Jiang, M.; Sun, Y.; Wu, X.; Huang, K.; Feng, S. Engineering Cu_2O/Cu@CoO Hierarchical Nanospheres: Synergetic Effect of Fast Charge Transfer Cores and Active Shells for Enhanced Oxygen Evolution Reaction. *Inorg. Chem. Front.* **2019**, *6*, 1660−1666.
(81) Xia, L.; Liu, G.; Wang, J.; Luo, S. Facile Synthesis of Micron-Sized Hollow Copper Spheres with ZSM-5 Molecular Sieve as a Template. *J. Raman Spectrosc.* **2009**, *40*, 876−880.
(82) Xiong, L.; Li, S.; Zhang, B.; Du, Y.; Miao, P.; Ma, Y.; Han, Y.; Zhao, H.; Xu, P. Galvanic Replacement-Mediated Synthesis of Hollow Cu_2O-Au Nanocomposites and Au Nanocages for Catalytic and SERS Applications. *RSC Adv.* **2015**, *5*, 76101−76106.
(83) Sui, Y.; Fu, W.; Yang, H.; Zeng, Y.; Zhang, Y.; Zhao, Q.; Li, Y.; Zhou, X.; Leng, Y.; Li, M.; Zou, G. Low Temperature Synthesis of Cu_2O Crystals: Shape Evolution and Growth Mechanism. *Cryst. Growth Des.* **2010**, *10*, 99−108.
(84) Trotochaud, L.; Head, A. R.; Pletincx, S.; Karslıoğlu, O.; Yu, Y.; Waldner, A.; Kyhl, L.; Hauffman, T.; Terryn, H.; Eichhorn, B.; Bluhm, H. Water Adsorption and Dissociation on Polycrystalline Copper Oxides: Effects of Environmental Contamination and Experimental Protocol. *J. Phys. Chem. B* **2018**, *122*, 1000−1008.

DOI: 10.1021/acs.chemmater.9b02240
Chem. Mater. 2019, 31, 8000−8011